

Article

A Solid Redox Mediator Analog as a Highly Efficient Catalyst for Na–O₂ Batteries

Qin-yin Shen¹, Jin-ling Ma^{1,*} , Ming-lu Li¹, Wei He¹, Ying-yue Tan¹, Peng-yu Zhou¹ and Yu Wang^{1,2,*}

¹ State Key Laboratory of Power Transmission Equipment & System Security and New Technology, Chongqing University, 174 Shazheng Street, Shapingba District, Chongqing 400044, China

² School of Chemistry and Chemical Engineering, Chongqing University, 174 Shazheng Street, Shapingba District, Chongqing 400044, China

* Correspondence: mjl201909@cqu.edu.cn (J.-l.M.); wangy@cqu.edu.cn (Y.W.)

Abstract: During the discharge of Na–O₂ batteries, O₂ is reduced and combines with Na⁺ to form an insulating solid sodium oxide on the cathode, which severely hinders the mass transfer path, resulting in high polarization voltage, low energy efficiency, and short battery life. Hereby, we proposed a novel illumination-assisted Na–O₂ battery in which bismuth vanadate (BiVO₄) with few defects and high surface areas was used as the catalyst. It showed that the charge overpotential under photo assistance reduced by 1.11 V compared with that of the dark state one. Additionally, the insulating sodium oxide discharge products were completely decomposed, which was the key to running Na–O₂ batteries over 200 cycles with a charge potential of no more than 3.65 V, while its counterpart (under dark condition) at 200 cycles had the charge potential higher than 4.25 V. The experiment combined with theoretical calculation shows that few defects, high surface areas, the altered electron transfer kinetics, and the low energy gap and low oxygen absorption energy of the (040) crystal face of monoclinic BiVO₄ play an important role in catalyzing oxygen reduction reaction (ORR) and oxygen evolution reaction (OER).



Citation: Shen, Q.-y.; Ma, J.-l.; Li, M.-l.; He, W.; Tan, Y.-y.; Zhou, P.-y.; Wang, Y. A Solid Redox Mediator Analog as a Highly Efficient Catalyst for Na–O₂ Batteries. *Batteries* **2022**, *8*, 227. <https://doi.org/10.3390/batteries8110227>

Academic Editors: Yu Li and Qiao Ni

Received: 28 September 2022

Accepted: 2 November 2022

Published: 9 November 2022

Publisher's Note: MDPI stays neutral with regard to jurisdictional claims in published maps and institutional affiliations.



Copyright: © 2022 by the authors. Licensee MDPI, Basel, Switzerland. This article is an open access article distributed under the terms and conditions of the Creative Commons Attribution (CC BY) license (<https://creativecommons.org/licenses/by/4.0/>).

Keywords: Na–O₂ batteries; BiVO₄ photocatalyst; photo-assistance; low overpotential; fast electron transfer

1. Introduction

In recent years, the environmental pollution and climate warming caused by the consumption of fossil energy cannot be ignored, so there is an urgent need to develop efficient and clean energy conversion and storage devices [1–4]. Na–O₂ batteries have attracted much attention because of their higher specific energy density and lower cost compared to lithium-ion batteries [5]. However, the disadvantage is that high charging potential is required to decompose the poorly soluble and well-insulating discharge products in Na–O₂ batteries, which limits their practical application [6]. This leads not only to low energy efficiency but also to the decomposition of electrolytes during cycling, thus reducing the cycle life of Na–O₂ batteries. Therefore, it is urgent and necessary to reduce the charging overpotential of Na–O₂ batteries [7–10].

In order to overcome the above problems of non-aqueous Na–O₂ batteries, great efforts have been made, such as developing the high electrocatalytic activity of catalysts/cathodes, using redox mediators. Carbon material is low cost, abundant, has high surface areas, and easily regulates morphology, whereas its intrinsic low catalytic activity limit it to being the matrix of the cathode [11,12]. Transition metal oxides are reported to have highly electrocatalytic activity, but the low conductivity compels them to organically combine with conductive agents, thus increasing preparation difficulty [13,14]. The noble metals such as high electrocatalytic catalysts can significantly reduce the overpotential in the absence of balance consideration between the high price and their large-scale use [15–17]. The soluble redox mediators as the most effective catalysts can largely reduce overpotential, but their

use is also accompanied by new problems, such as the anode degradation from the shuttle effect and the continuously declining catalytic activity as redox mediators decrease [12,18]. Therefore, developing a catalyst with the catalytic activity comparable to that of redox mediators with no detriment to the anode is very important and essential.

Photocatalysts introduced into Li–O₂ batteries displayed a remarkable effect, similar to redox mediators on reducing polarization [19,20]. Upon discharge, the photocatalyst generates electron and hole by illumination, then the electron reduces oxygen and the hole accepts the electron from the anode. The photocatalyst returns to its original state. On charge, the produced hole from photocatalyst by illumination will extract the electron of discharge products; the electron from the photocatalyst will run to anode to reduce metal ion through external circuits. The function of photocatalyst can be illustrated as shown in Supplementary Materials Figure S1. No matter the discharge or charge, the structure of photocatalysts will be retained.

Now, many photocatalysts have been studied in Li–O₂ batteries, while they have not been explored in Na–O₂ batteries. Even though the battery reaction mechanism is similar between Li–O₂ and Na–O₂ batteries, there are some differences between them, such as the discharge products. The elucidation of the relationship between catalytic activity and the crystal structure and morphology of photocatalysts is meaningful to improve the performance of Na–O₂ batteries, which can also simplify the solar energy storage in Na–O₂ batteries.

Bismuth vanadate (BiVO₄) is an attractive photocatalyst due to its low band gap, non-toxicity, resistance to corrosion, and good stability [21]. There are three crystalline phases reported for synthetic BiVO₄. Only monoclinic BiVO₄ shows a greater photocatalytic performance owing to the lone pair distortion of Bi 6s orbital [22,23]. Varying the synthesis methods and conditions can modulate the particle size, crystallinity, and morphology of BiVO₄ [24,25].

Herein, the smaller size of the optimized crystal face exposed BiVO₄ was synthesized by a simple hydrothermal method through adjusting pH of the precursor. The small sized and clean BiVO₄ showed a larger surface area. The exposed (040) crystal face is easily radiated and delivers a fine oxygen adsorption-desorption capability. When combined with carbon nanotubes (CNTs), the generated electron from BiVO₄ induced by light gained a facilitated transfer, boosting the reaction kinetics of Na–O₂ batteries. These enable Na–O₂ batteries with a huge overpotential drop by 1.11 V and more than 200 cycles life, demonstrating the great use potential of BiVO₄.

2. Materials and Methods

2.1. Bismuth Vanadate Preparation

First, 5 mmol Bi(NO₃)₃·5H₂O was dissolved in 20 mL 4 mol/L HNO₃ solution, and 5 mmol NH₄VO₃ was dissolved in 20 mL 4 mol/L sodium hydroxide solution by vigorous stirring for 2 h. Secondly, the above solutions were mixed and continuously stirred for 30 min to obtain a homogeneous orange yellow solution. NH₃·H₂O or CH₃COOH was used to adjust the pH of the solution. After that, the obtained mixture was transferred into a Teflon-lined stainless-steel autoclave and then was heated at 160 °C for 12 h. After heating, the autoclave was naturally cooled down to room temperature and the yellow precipitate was formed. Finally, the precipitate was collected by filtration, then washed by deionized water and ethanol three times, respectively, and finally dried at 80 °C in an oven overnight to obtain BiVO₄.

2.2. The Electrode Preparation

BiVO₄, carbon nanotubes, and polyvinylidene fluoride were mixed in a mass ratio of 75:15:10 and then ground in a grinding miller with 2 mL NMP for 30 min. Then, the mixture was evenly coated on the carbon paper, and was dried at 80 °C. After that, the dried carbon paper was transferred into vacuum oven to dry at 90 °C for 20 h. Finally, the dried carbon paper was punched into 12 mm in diameter as the BiVO₄ cathode with the

mass loading of 0.6 mg. For the CNTs cathode preparation, it was the same as that of BiVO₄ one, except for the step that substituted BiVO₄ with CNTs.

2.3. The Assembly of Na–O₂ Batteries

Electrolyte solvent, tetraethylene glycol dimethyl ether (TEGDME), was dried by activated molecular sieves (4 Å type) until the water content below 10 ppm. NaCF₃SO₃ as the salt of electrolyte was dried in a vacuum oven at 80 °C for 12 h. The electrolyte was formulated by dissolving NaCF₃SO₃ into TEGDME (H₂O < 10 ppm) to obtain 0.5 M NaCF₃SO₃/TEGDME electrolyte. All Na–O₂ cells were assembled with 2025-type coin cells in a glove box under argon atmosphere (H₂O < 1 ppm, O₂ < 1 ppm). A sodium metal foil processed from the Na bulk as the anode (Φ = 12 mm), a glass fiber separator, the above cathode, and 80 μL 0.5 M NaCF₃SO₃/TEGDME electrolyte were combined in sequence (press pressure: 800 Pa). Next, the batteries were purified by pumping vacuum and ventilating with high-purity O₂ alternatively for three times. After that, the pure batteries were filled with O₂ under 1 atm and then sealed and stood for 3 h for subsequent electrochemical tests.

2.4. Characterization

Powder X-ray diffraction (XRD) measurements of BiVO₄ and cathode were conducted on PANalytical X'Pert Powder with Cu Kα radiation (Spectris Pte. Ltd, The Netherlands). The morphology of BiVO₄ and discharge products were analyzed by scanning electron microscope (SEM, JEOL JSM-6700, Japan). The structure of BiVO₄ was gained on a FEI Tecnai G2 F30 transmission electron microscope (TEM, Thermo Fisher Scientific CD Ltd, Czech Republic) with the sample deposited on a copper grid. Raman spectra were obtained at a laser wavelength of 532 nm by the Horiba LabRAM HR evolution microscope (HORIBA Jobin Yvon S.A.S. France). Approximately 5% of the maximum laser power (13 mW) was used for preventing laser from damaging the CNTs. X-ray photoelectron spectroscopy (XPS) of BiVO₄ was tested on an ESCALAB 250Xi (Thermo Fisher Scientific, USA). The UV-Vis diffuse reflectance spectra were collected on a UV-2550PC spectrophotometer (Shimadzu, Japan), using BaSO₄ as the reference with a wavelength range of 200–800 nm. Nitrogen adsorption-desorption isotherms for measuring specific surface area were obtained on a multistation surface and porosity analyzer max-II (MicrotracBEL, Japan).

2.5. Electrochemical and Photoelectrochemical Measurement of Na–O₂ Batteries

Electrochemical impedance spectroscopy (EIS) and linear sweep voltammetry (LSV) measurements of Na–O₂ cells were performed on a Biologic SP-200 electrochemical workstation with an EIS frequency range of 10⁶ to 10^{−2} Hz. For the LSV tests, a two-electrode setup (the 2025-type coin Na–O₂ battery) was used wherein the sodium anode was not only used as the counter but also the reference electrode, and BiVO₄/CNTs cathode was the working electrode. Galvanostatic discharge–charge measurements of Na–O₂ batteries were performed at the voltage ranging from 1.8 to 4.5 V on a LAND CT3001A multi-channel battery testing instrument. The Na–O₂ cells were discharged to 1.8 V to obtain the maximum discharge capacity under pure oxygen atmosphere. The cycling tests were controlled with the confined capacity and current density. A 300 W Xe-lamp light source with the power of 300 mW cm^{−2} and wavelength range from 220–1200 nm was used to provide irradiation for the electrochemical performance test of Na–O₂ cells as schemed in Supplementary Materials Figure S2 (the distance between the light source and the Na–O₂ cell is 20 cm).

2.6. Computational Methods

Density functional theory (DFT) calculations were carried out by the Vienna Ab-initio Simulation Package (VASP) [26]. The projected augmented wave method was used to describe the valence electron–ion interaction. A generalized gradient approximation by the GGA-PBE functional was used to calculate the electron exchange and correlation energies. In consideration of photoelectrons' delocalization in the GGA-PBE calculation, the DFT + U

method was adopted in this work using a Hubbard-type correction by setting 3 eV $U_{\text{eff},V}$ for V 3d orbital [27]. The force tolerance lower than 0.01 eV/Å and the energy difference lower than 10^{-5} eV were set for the structure optimization. The cutoff energy was set to be 400 eV. The bulk structure optimization was done in a $6 \times 3 \times 9$ Monkhorst–Pack (MP) k-point mesh with lattice parameters of $a = 7.33790$ Å, $b = 11.74769$ Å, and $c = 3.66882$ Å [28]. The non-polar (110), (121), and (040) surface slabs with three layers in stoichiometry of BiVO_4 were generated from the optimized bulk lattice. Monkhorst–Pack (MP) k-point mesh is $5 \times 4 \times 1$ for (110), $2 \times 2 \times 1$ for (121), and $5 \times 5 \times 1$ for (040), respectively. The vacuum space along the c direction was set to be 15 Å and the thickness of these slab were 22–28 Å. For slab calculations, dipole correction was taken into account. The adsorption model was composed of a 2×2 for (040) slab, and 2×1 supercell for (110) slab to avoid the interactions of adsorbed O_2 .

3. Results

The BiVO_4 prepared in different pH value of the precursor solution was referred to as BV- n , wherein BV and n meant BiVO_4 and pH, respectively. X-ray diffraction (XRD) was conducted to determine the crystalline phase. Figure 1a shows that all diffraction peaks are indexed to monoclinic BiVO_4 (JCPDS No. 14-0688) and no other impurity phase appears. Notably, the BV-6 exhibits more intense diffraction peaks than the BV-4 and BV-8, indicating its highest crystallinity, which is beneficial for its stability. The SEM image shows the BV-4 with a distinct polyhedral shape, smooth surface, and dispersive size distribution, while the BV-6 displayed a focused size distribution, which meant more crystal faces exposure for the increased diffraction peaks intensity, as shown in Figure 1b,c. When the pH was 8 (Figure 1d), the polyhedral shape BiVO_4 disappeared, but it became rough, slender, and needle-like, along with branching accompanied by many aggregated particles. The high-resolution TEM image (Figure 1e) showed an obvious lattice fringe of 0.292 nm, indexed to 040 crystal face, which also implied (040) a stable crystal face. Compared with the BV-4 and BV-8, the BV-6 showed a smaller size of about 355 nm, which implied a higher surface area (Supplementary Materials Figure S3). The BET measurement (Supplementary Materials Figure S4) shows that the BV-6 ($4.52 \text{ m}^2 \text{ g}^{-1}$) has a higher surface area than the BV-4 ($3.63 \text{ m}^2 \text{ g}^{-1}$) and BV-8 ($2.15 \text{ m}^2 \text{ g}^{-1}$). This is also consistent with the SEM image shown.

The valence states and composition of BiVO_4 were investigated by XPS. The survey XPS spectrum showed Bi, V, and O elements in BiVO_4 (Supplementary Materials Figure S5). The deconvolution O 1s XPS showed binding energies centered at 529.0 and 531.7 eV, which are associated with lattice oxygen and chemical adsorption oxygen, respectively (Figure 1f). It is well known that chemical adsorption O results from the positive charged oxygen vacancies [29]. In the three samples, the BV-6 has the largest chemical adsorption O content, possibly implying a number of oxygen vacancies. The binding energies for V 2p XPS lie at 516.5 and 524.1 eV, which was attributed to V^{5+} (Figure 1g). For the Bi 4f XPS spectra (Figure 1h) of the three samples, the binding energies concentrated at around 164.5 and 159.2 eV attributed to the signals of Bi 4f_{7/2} and Bi 4f_{5/2}, respectively, which was the feature of Bi^{3+} species.

Raman spectra in Figure 1i presents nearly no band shift at 366 and 326 cm^{-1} related to the symmetric and asymmetric bending modes of V–O in VO_4 tetrahedra, respectively. The band at 819 cm^{-1} corresponding to symmetric V–O stretching mode appears with a slight blue shift for BiVO_4 prepared at high pH conditions, revealing less defect formation as pH increases [30].

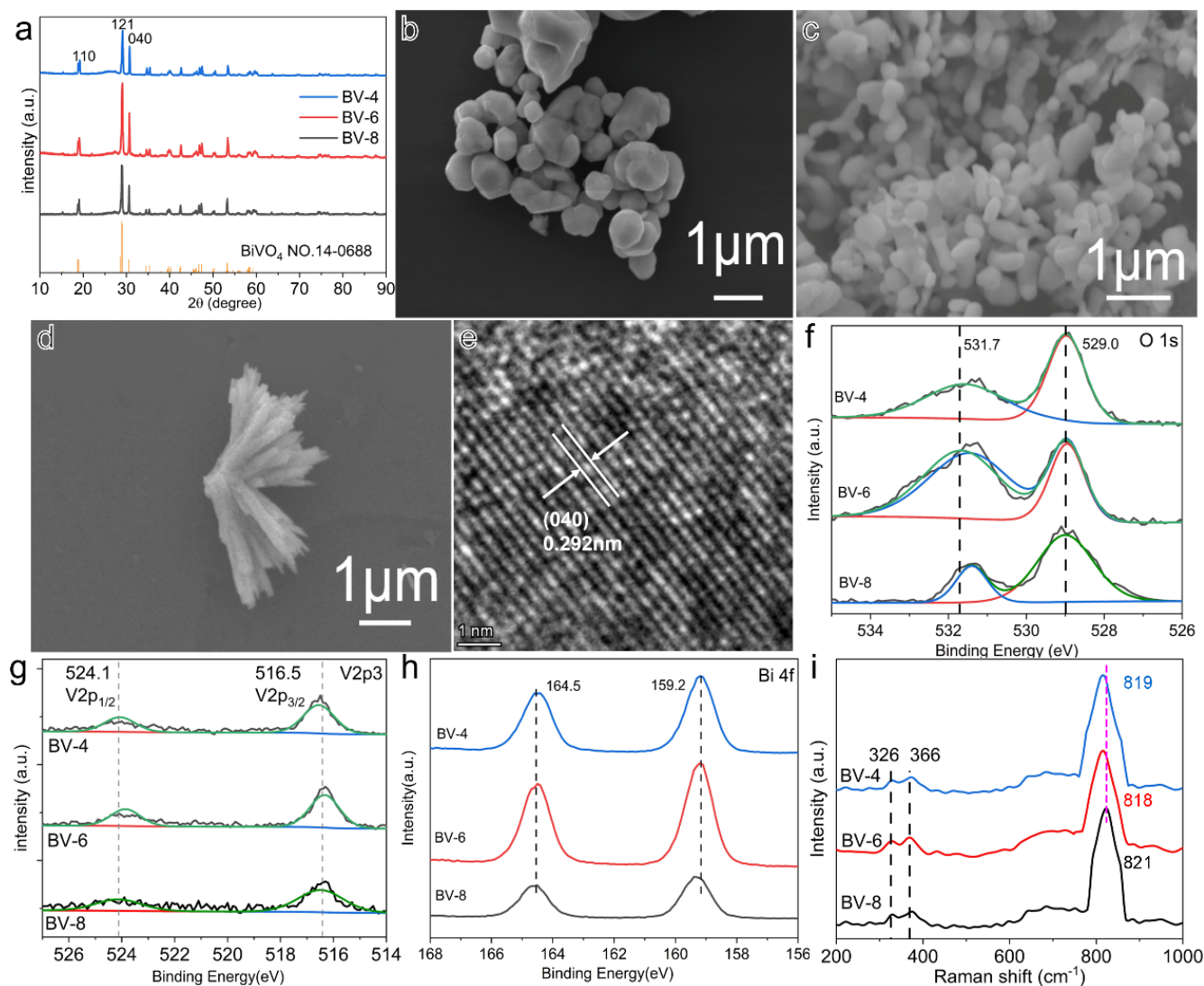


Figure 1. (a) XRD patterns of BiVO_4 ; SEM images the of (b) BV-4, (c) BV-6, and (d) BV-8, (e) HRTEM image of the BV-6; (f) O 1s XPS, (g) V 2p XPS, (h) Bi 4f XPS spectra, and (i) Raman spectra of BiVO_4 .

The optical absorption properties of the photocatalysts are the key factors affecting their photocatalytic performance. To get optical absorption capability of BiVO_4 , the UV-vis measurement was conducted as shown in Figure 2a. Compared with the BV-4 and BV-8, BV-6 obtained the largest absorption. The energy band gap (E_g) can be obtained from the Tauc plot, which can be derived from UV-vis spectrum (Supplementary Materials Figure S6). E_g can be determined by the equation, $h\nu\alpha = (h\nu - E_g)^n$, wherein h is the Planck constant, ν is the photon frequency, α is the constant of proportionality, and n defines the nature of the electron leap ($n = 0.5$ for the direct; $n = 2$ for the indirect). For our case, BiVO_4 is an indirect semiconductor, so the n should be 2 [31,32]. Therefore, the fitted E_g for the BV-6 was 2.46 eV, almost close to the theoretical value of monoclinic phase BiVO_4 [33,34]. The linear sweep voltammetry (LSV) curves presented in Figure 2b show that the BV-6 electrode obtains the higher reduction current density, indicating more reduction reactions on the BV-6 cathode under illumination. Additionally, the onset ORR potential of the BV-6 was higher than the others. Tafel slope, reflecting the ORR reaction kinetics, was determined according to the LSV curves of ORR. It displays the BV-6 with a smaller Tafel slope value (60.3 mV dec^{-1}) than the BV-4 (103 mV dec^{-1}) and BV-8 (161 mV dec^{-1}), indicating that BV-6 has superior ORR reaction kinetics (Figure 2c). The transient photocurrent electrochemical impedance spectroscopy (EIS) measurement was conducted in 0.1 M potassium phosphate (K-Pi)

buffered electrolyte (pH 7.0) by taking $\text{BiVO}_4/\text{CNTs}$ as the working electrode, Pt foil as the counter electrode, and the saturated calomel electrode as the reference electrode shown in Figure 2d and Table S1. The semi-circle in EIS plot at high frequency represents the interface charge transfer resistance. The smaller the semi-circle, the lower the interfacial impedance for the faster charge transfer. Obviously, the BV-6 obtained the lowest impedance, showing its fast charge transfer [35,36]. Additionally, the LSV of the OER process in Figure 2e also exhibited a higher OER current density for the BV-6 under the potential range from 2.4~3.4 V under illumination, showing a more favorable OER reactions on the BV-6 cathode. Moreover, the according Tafel slopes deduced from LSV of OER showed that the BV-6 had a smaller value than the BV-4 and BV-8, indicating that the BV-6 had faster OER kinetics (Figure 2f).

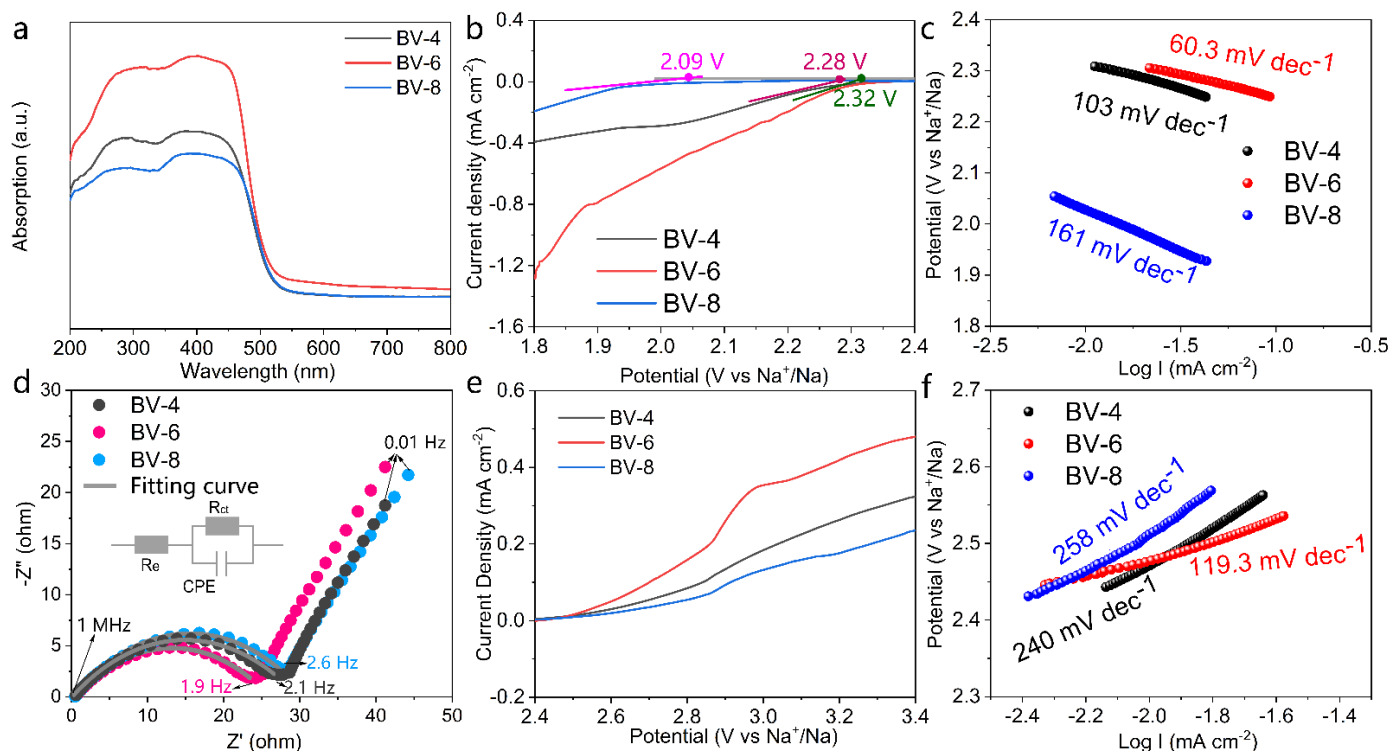


Figure 2. UV-visible absorption spectra (a), LSV curves for ORR at a scan rate of 0.1 mV s^{-1} (b), the corresponding Tafel slope for ORR (c), EIS (d), LSV curves for OER at a scan rate of 0.1 mV s^{-1} (e), and the corresponding Tafel slope for OER (f) of the $\text{BiVO}_4/\text{CNTs}$ electrode under illumination.

To elucidate the relationship between the photocurrent response of BiVO_4 and its performance of Na-O_2 batteries, the three BiVO_4 samples mixed with conductive CNTs were used as the cathodes to test in Na-O_2 batteries. Figure 3a shows the free discharge curves. It showed that the BV-6 delivered the largest discharge capacity as well as the discharge potential, while the BV-4 obtained the second-high discharge potential and the lowest discharge capacity due to its low specific surface area. As for the BV-8, it had the third highest discharge capacity, and its discharge potential is close to that of the BV-4. This result showed a positive correlation between the photocurrent response and performance of Na-O_2 batteries when using BiVO_4 . Based on the above results, we chose the BV-6 as the optimized photocatalyst to further study its performance and catalytic mechanism. The rate capability of Na-O_2 batteries in Figure 3b showed that as the discharge current density increased, the polarization also increased because of mass transportation constraints. Interestingly, the discharge potential for the BV-6 electrode under illumination still maintained above 1.9 V at the current density of 1800 mA g^{-1} , far exceeding that of the cell without illumination (1.13 V). The possible reason for this trend is the more facilitated electron transfer of the BV-6 under illumination.

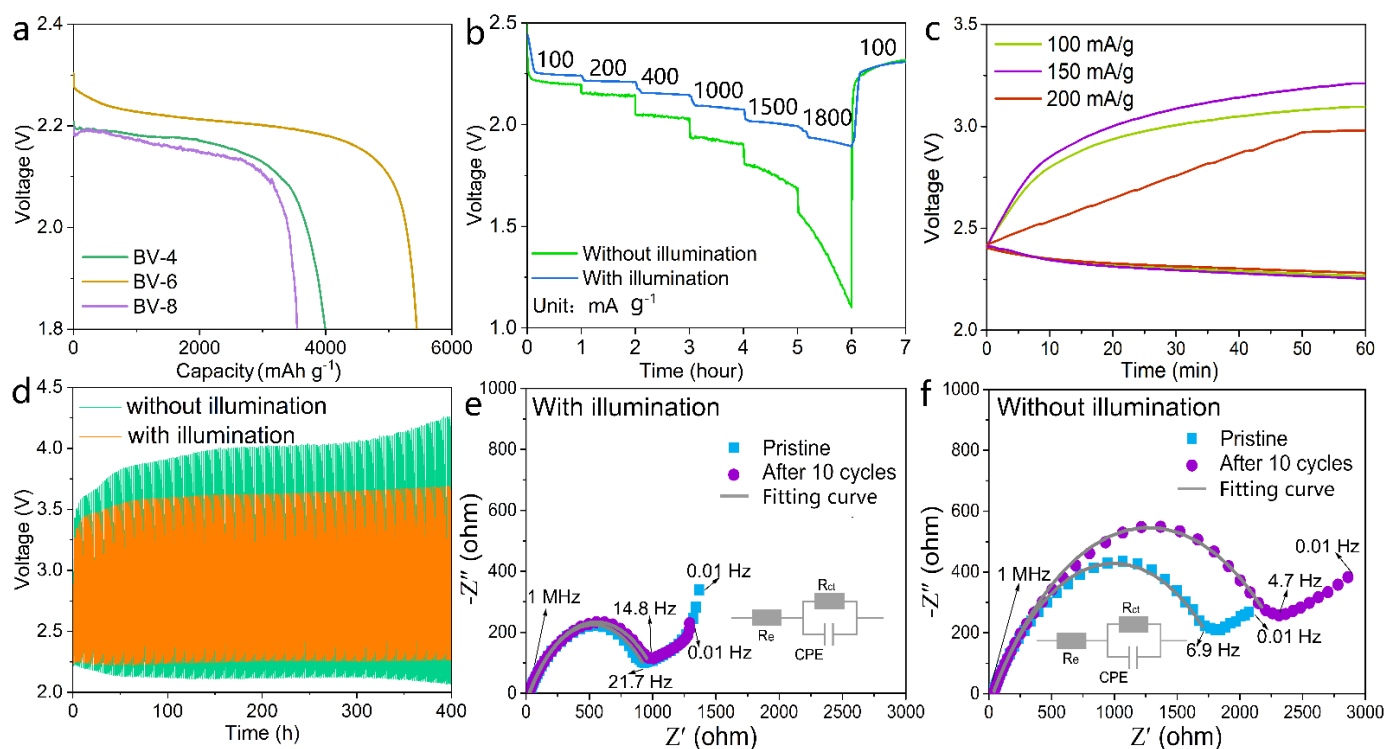


Figure 3. (a) The free-discharge curves, (b) the rate capability, (c) the discharge/charge curves at different current densities, (d) the cycling performance, and the EIS of the Na–O₂ batteries using BV-6/CNTs cathode under (e) illumination, (f) no illumination.

Figure 3c is the discharge and charge curves of Na–O₂ batteries at different current densities using the BV-6 as the catalyst. Specifically, the discharge potential was 2.29 V at the discharge current density of 100 mA g⁻¹. As the current density increased to 150 mA g⁻¹, the discharge potential remained at 2.27 V, and when the current density continued to increase to 200 mA g⁻¹, the discharge potential was still kept at 2.32 V. The small discharge potential drop indicates the BV-6 a high catalytic activity. Similarly, the charging potential increased from 3.08 V to 3.2 V as the current density increased from 100 to 150 mA g⁻¹, much lower than the ever-reported solid catalysts (Supplementary Materials Table S2).

Figure 3d and Figure S7 show the cycling performance of Na–O₂ cells with the BV-6 as the catalyst evaluated by a galvanostatic method. It can be observed that under illumination at the current density of 200 mA g⁻¹, the discharge potential displayed a constant value (2.26 V) regardless of the cycles increasing, while without illumination, it was obviously lower under the same cycle and reduced from 2.25 V at the initial to 2.08 V at the final. This demonstrated that the fast production of electron from photocatalysts facilitated battery reactions, thus reducing the polarization during discharge. In charge, the potential of Na–O₂ batteries under illumination underwent an ignorable increase as cycling proceeded. Moreover, it remained at around 3.65 V, far lower than 4.25 V. Compared with illumination assistance, the charge potential under dark conditions experienced remarkable increase from 3.5 at the initial to 4.25 V at the final. The high charge potential would threaten the stability and reduce the energy efficiency of battery [6]. It is easy to find that introduced BiVO₄ not only improves the discharge potential, but also reduces the charge polarization, demonstrating its high photocatalytic activity towards the reactions of Na–O₂ batteries.

The discharge–charge curves of Na–O₂ batteries at light-on-light-off was also measured (Supplementary Materials Figure S8). During 0–26 h, the battery was operated at light-on and its potential rose slowly. Subsequently, the light was off and the battery showed a rapid discharge and charge potential increase, which was probably due to the inhibiting catalytic activity of the BV-6 in the absence of light. When the light was on again the discharge and charge potential appeared increased, but it was still lower than that of no light-on

cell. The slowly increased overpotential possibly resulted from the accumulated products covering the photocatalysts, thus inhibiting the catalytic activity. This can be verified by the varied EIS of 2025-type coin Na–O₂ cells with a two-electrode setup during different electrochemical process (Figure 3e,f and Table S1). The semi-circle in EIS is attributed to the interfacial resistance and charge transfer resistance. Before being discharged, the illuminated batteries showed a smaller semi-circle than that of the dark one, indicating the lower interfacial resistance and charge transfer resistance of BiVO₄ electrode assisted by light. When the batteries ran 10 cycles under light on and light off, respectively, the EIS results showed that, compared with the pristine one, the resistance of the cell after 10 cycles under illumination delivered an ignorable rise, while that of the light-off one had an apparent increase. This difference possibly resulted from the increased interfacial resistance caused by the undecomposed products coated the conductive cathode.

To figure out the reaction of Na–O₂ batteries using BiVO₄, the evolution of discharge products was recorded. Figure 4a showed the discharged BiVO₄ electrode. Compared with the pristine BiVO₄ electrode with very few particles (Supplementary Materials Figure S9), the discharged one was covered by ball-liked discharge products constructed by accumulated particles. After charging, these ball-liked products disappeared, indicating their decomposition. Compared with that of Na–O₂ cells without light assistance (Figure 4b), the size of the discharge products became significantly smaller with light assistance, thus making them easier to decompose. The XRD patterns of the discharged electrode showed that the diffraction peaks corresponding to Na₂O₂ appeared after being discharged under both illumination and non-illumination conditions, indicating that the BiVO₄ photocatalysts did not change the reactions of the Na–O₂ cell. The peaks of Na₂O₂ were no longer present after being charged under illumination, showing the decomposition of sodium peroxide (Figure 4c). Raman testing is an efficient way to characterize a material, no matter whether it is crystalline or amorphous. It was employed to further analyze the composition of the discharge products (Figure 4d). It showed the mixed products of NaO₂ and Na₂O₂, consistent with the ever-reported battery reactions, namely first generation of NaO₂ by electrochemical reaction accompanied with the subsequent Na₂O₂ formation by chemical conversion [36,37]. It should also be noted that the signals of NaO₂ were stronger under illumination than non-illumination. The stronger signal of NaO₂ on the illuminated BiVO₄ electrode possibly resulted from fast electron transfer facilitated to the kinetics of battery reactions, thus promoting the production of NaO₂ just as previously reported [37,38]. As for the absent signal of NaO₂ in XRD patterns of the discharged BiVO₄ electrode, it was possibly due to the poor crystalline NaO₂. In fact, the most reported signal was the strong XRD signal of NaO₂, which always appeared at the size of NaO₂ approximated to several micron. In our case, according to SEM image, the size of NaO₂ was less than 1 μm and its morphology was not cubic. Therefore, it is rational for the absent signal of NaO₂ in XRD.

The stability of BiVO₄ in Na–O₂ batteries is key to functioning the long-term catalytic activity, so we tracked the variation of catalysts and cathodes. XRD patterns of the BiVO₄/CNTs electrode after 10 cycles were in line with that of the initial one (Figure 4c). The element mapping images of the cycled BiVO₄ electrode showed the distinct shape constituted by Bi, V, and O elements (Supplementary Materials Figure S10). The focused O element is different from the C element with evident dispersion, further showing no oxidation of the CNTs. The HRTEM image of the cycled BiVO₄ showed a 0.292 nm lattice fringe (Supplementary Materials Figure S11), consistent with the initial BiVO₄, indicating the stability of BiVO₄.

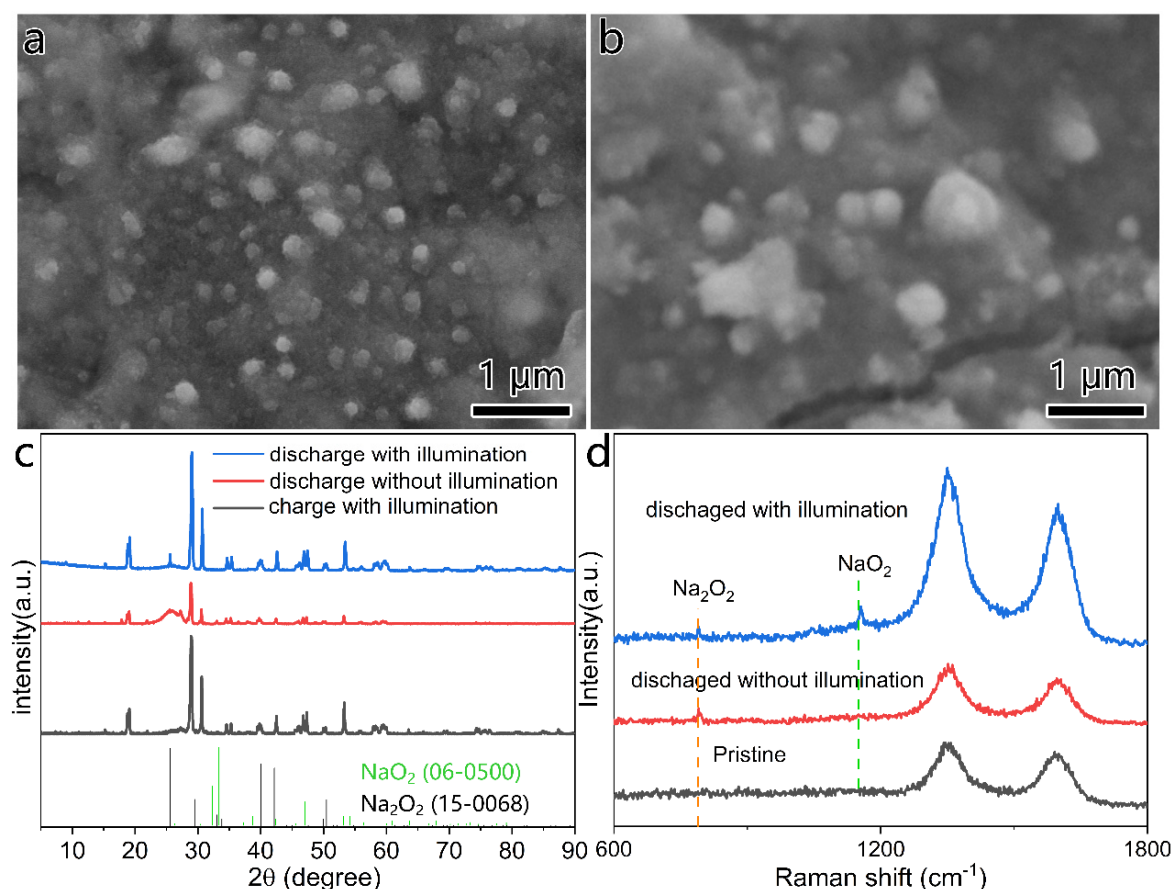


Figure 4. SEM images for the discharged BV-6 cathode under (a) illumination, (b) no illumination; (c) XRD patterns; (d) Raman spectra for the BV-6/CNTs cathode operated in Na-O₂ batteries.

To gain insights into the photocatalytic mechanism of BiVO₄, density functional theory calculations were carried out. Catalytic reaction always occurs on the surface of a material, so finding the exposed surface is useful to study the catalytic mechanism. The lower the surface energy, the easier the crystal face is exposed. The common surface energy calculation is based on the following equation:

$$\gamma = (E_{\text{total}} - nE_{\text{bulk}})/2A \quad (1)$$

where γ is the surface energy of the facet, E_{total} is the total energy of the relaxed BiVO₄ surface slab, E_{bulk} is the total energy of BiVO₄ bulk unit cell, n is the number of the bulk BiVO₄ unit in the slab, and A is the surface area of the slab. According to experimental results, the observed facet by HRTEM and the high intense facets from XRD were selected to be calculated. As shown in Supplementary Materials Table S3, it shows that the (040) surface has the lowest surface energy of 0.76 J/m² and is therefore the most stable facet of BiVO₄, in line with the HRTEM result. The electronic structures of photocatalyst are related to photocatalysis performance. Therefore, the density of state for all facets are calculated by using the DFT + U method. The E_g can be obtained by the conduction band minimum subtracting the valence band maximum. The E_g of the bulk BiVO₄ is 2.4 eV verified by many reports [39,40]. In our work, it can be found that only the stable (040) surface demonstrated an E_g (2.03 eV) closed to the bulk one (Figure 5a–c). O₂ absorption on BiVO₄ is a key step for its subsequent catalyzing of ORR. The experimental results showed a few oxygen defect existences in the prepared BiVO₄. The (110), (121), and (040) facets with defects were selected to study their absorption for O₂. The adsorption configurations were shown in Figure 5d–i, and the order of adsorption energy is (110) < (040) < (121). The smaller the adsorption energy, the stronger the adsorption [41]. However, it is a fact that

the stronger the adsorption, the harder the desorption. O₂ desorption is also key to the charge of Na–O₂ battery. Therefore, the stable (040) facet with a moderate O₂ adsorption, as well as the E_g close to the experimental result, possibly plays an important role for the improved performance of Na–O₂ batteries.

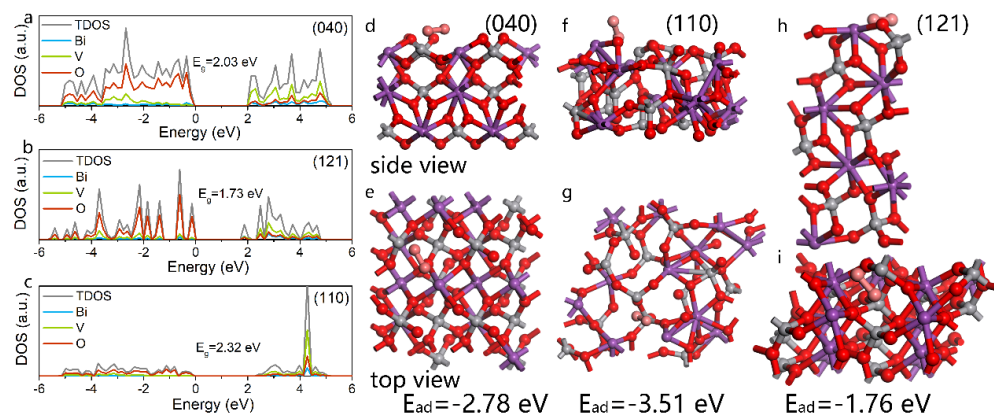


Figure 5. The density of states for the (a) (040), (b) (121), (c) (110) slab; the side view of a O₂ molecule adsorbed on (d) (040), (f) (110), (h) (121) slab, and the top view of a O₂ molecule adsorbed on (e) (040), (g) (110), and (i) (121) slab.

4. Conclusions

In summary, a well-crystalline, uniform-sized BiVO₄ with high specific surface areas was prepared as a photocatalyst to use in Na–O₂ battery. It is found that the photoelectric performance of BiVO₄ is positively related to the battery performance. The Na–O₂ batteries assembled with BiVO₄ under photo-assistance can be continuously cycled for more than 200 times with its charge potential lower than 3.65 V, much lower than that of the dark one (4.25 V). Moreover, the discharge potential is still maintained at 1.9 V even though the discharge currents density is up to 1800 mA g⁻¹. Additionally, the high active specific surface areas are good for improving capacity. The experiment associated with theory calculation demonstrates that the high crystallinity, specific surface, and the low E_g, namely facilitating the separation of the electron and hole, are beneficial for photoelectric responses and electron transfers in batteries, which improves the battery reaction kinetics. On an atomic scale, the exposed (040) facet with low surface energy presents a low energy gap and fine oxygen absorption capability, functioning as a positive impact on catalyzing ORR and OER.

Supplementary Materials: The following supporting information can be downloaded at: <https://www.mdpi.com/article/10.3390/batteries8110227/s1>; Figure S1: The scheme for the function of photocatalyst in Na–O₂ battery; Figure S2: The scheme for (a) the construction of Na–O₂ battery testing on (b) illumination and (c) no illumination; Figure S3: SEM image, and the corresponding particle size distribution plot for the (a,d) BV-4, (b,e) BV-6, (c,f) BV-8; Figure S4: Nitrogen adsorption-desorption isotherm of the BiVO₄; Figure S5: The survey XPS spectra of the BiVO₄; Figure S6: Tauc plot for the three BiVO₄ samples; Figure S7: The cycling performance of the Na–O₂ batteries using the BV-6/CNTs cathode under illumination at current density of 500 mA g⁻¹; Figure S8: Discharge–charge curves of Na–O₂ cells with BV-6/CNTs cathode at a current density of 150 mA g⁻¹ under intermittent illumination and no illumination conditions; Figure S9: SEM image of the (a) pristine, and (b) charged BV-6/CNTs cathode in Na–O₂ cell under illumination; Figure S10: TEM element mapping of the (a) Bi, (c) O, (d) V, and (d) C for the cycled BV-6/CNTs cathode; Figure S11: TEM image of the BV-6 after cycling (insert: the enlarged view of lattice stripes); Table S1: The fitted value from Nyquist plot from Figures 2d and 3e,f; Table S2: Electrochemical performance comparisons between this work and the reported catalysts/cathode in Na–O₂ batteries; Table S3: Area of the surface unit cell A in Å², surface energy σ in J m⁻², surface relaxation energy E_{rel} and surface cleavage energy E_{cle} in eV, energy gap E_g and and O₂ molecule adsorption energy E_{adsorb} on different surfaces in eV. σ = (E_{rel} + E_{cle})/A*16.02. References [42–46] are cited in the supplementary materials.

Author Contributions: Q.-y.S. conceptualization, methodology, validation, investigation, data curation, writing—original draft, writing—review and editing; M.-l.L. and W.H. validation, data curation, formal analysis; Y.-y.T. and P.-y.Z. software, investigation, data curation; J.-l.M. and Y.W. conceptualization, supervision. All authors have read and agreed to the published version of the manuscript.

Funding: This research received no external funding.

Data Availability Statement: Not applicable.

Acknowledgments: The authors are grateful for the support received from the National Natural Science Foundation of China (NSFC, Grant No. 22005041), the State Key Laboratory of Mechanical Transmissions Project (SKLMT-ZZKT-2017M11), the Fundamental Research Funds for the Central Universities (2022CDJXY-007), the 111 Project of the Ministry of Education, China (No. B08036).

Conflicts of Interest: The authors declare no conflict of interest.

References

1. Fang, R.; Chen, K.; Yin, L.; Sun, Z.; Li, F.; Cheng, H.-M. The Regulating Role of Carbon Nanotubes and Graphene in Lithium-Ion and Lithium-Sulfur Batteries. *Adv. Mater.* **2019**, *31*, 1800863. [[CrossRef](#)] [[PubMed](#)]
2. Zhang, C.; Shen, L.; Shen, J.; Liu, F.; Chen, G.; Tao, R.; Ma, S.; Peng, Y.; Lu, Y. Anion-Sorbent Composite Separators for High-Rate Lithium-Ion Batteries. *Adv. Mater.* **2019**, *31*, 1808338. [[CrossRef](#)] [[PubMed](#)]
3. Reddy, M.V.; Mauger, A.; Julien, C.M.; Paoletta, A.; Zaghbi, K. Brief History of Early Lithium-Battery Development. *Materials* **2020**, *13*, 1884. [[CrossRef](#)] [[PubMed](#)]
4. Yu, C.; Ganapathy, S.; Van Eck, E.R.H.; Wang, H.; Basak, S.; Li, Z.; Wagemaker, M. Accessing the bottleneck in all-solid state batteries, lithium-ion transport over the solid-electrolyte-electrode interface. *Nat. Commun.* **2017**, *8*, 1086. [[CrossRef](#)] [[PubMed](#)]
5. Zheng, Z.; Wu, C.; Gu, Q.; Konstantinov, K.; Wang, J. Research Progress and Future Perspectives on Rechargeable Na-O₂ and Na-CO₂ Batteries. *Energy Environ. Mater.* **2021**, *4*, 158–177. [[CrossRef](#)]
6. Benti, N.E.; Gurmesa, G.S.; Geffe, C.A.; Mohammed, A.M.; Tiruye, G.A.; Mekonnen, Y.S. Sodium-ion diffusion studies of the cathode-electrolyte interfaces (Na_xO₂@Na₂CO₃, x = 1 and 2) and discharge products of non-aqueous rechargeable sodium-air batteries. *J. Mater. Chem. A* **2022**, *10*, 8501–8514. [[CrossRef](#)]
7. Kang, Y.; Wang, S.; Zhu, S.; Gao, H.; Hui, K.S.; Yuan, C.-Z.; Yin, H.; Bin, F.; Wu, X.-L.; Mai, W.; et al. Iron-modulated nickel cobalt phosphide embedded in carbon to boost power density of hybrid sodium-air battery. *Appl. Catal. B-Environ.* **2021**, *285*, 119786. [[CrossRef](#)]
8. Kim, S.; Jung, Y.; Park, J.; Hong, M.; Byon, H.R. Sodium fluoride-rich solid electrolyte interphase for sodium-metal and sodium-oxygen batteries. *Bull. Korean Chem. Soc.* **2021**, *42*, 1519–1523. [[CrossRef](#)]
9. Ma, J.; Li, Y.; Grundish, N.S.; Goodenough, J.B.; Chen, Y.; Guo, L.; Peng, Z.; Qi, X.; Yang, F.; Qie, L.; et al. The 2021 battery technology roadmap. *J. Phys. D-Appl. Phys.* **2021**, *54*, 183001. [[CrossRef](#)]
10. Zheng, Z.; Jiang, J.; Guo, H.; Li, C.; Konstantinov, K.; Gu, Q.; Wang, J. Tuning NaO₂ formation and decomposition routes with nitrogen-doped nanofibers for low overpotential Na-O₂ batteries. *Nano Energy* **2021**, *81*, 105529. [[CrossRef](#)]
11. Benti, N.E.; Tiruye, G.A.; Mekonnen, Y.S. Boron and pyridinic nitrogen-doped graphene as potential catalysts for rechargeable non-aqueous sodium-air batteries. *Rsc Adv.* **2020**, *10*, 21387–21398. [[CrossRef](#)] [[PubMed](#)]
12. Munuera, J.M.; Paredes, J.I.; Enterría, M.; Villar-Rodil, S.; Kelly, A.G.; Nalawade, Y.; Coleman, J.N.; Rojo, T.; Ortiz-Vitoriano, N.; Martínez-Alonso, A.; et al. High Performance Na-O₂ Batteries and Printed Microsupercapacitors Based on Water-Processable, Biomolecule-Assisted Anodic Graphene. *ACS Appl. Mater. Interfaces* **2020**, *12*, 494–506. [[CrossRef](#)] [[PubMed](#)]
13. Liu, Y.; Chi, X.; Han, Q.; Du, Y.; Yang, J.; Liu, Y. Vertically self-standing C@NiCO₂O₄ nanoneedle arrays as effective binder-free cathodes for rechargeable Na-O₂ batteries. *J. Alloys Compd.* **2019**, *772*, 693–702. [[CrossRef](#)]
14. Changfan, X.; Xin, F.; Jing, Z.; Jiayi, C.; Feng, L. Progress for Metal-CO₂ Batteries: Mechanism and Advanced Materials. *Prog. Chem.* **2020**, *32*, 836.
15. Jeong, Y.S.; Park, J.-B.; Jung, H.-G.; Kim, J.; Luo, X.; Lu, J.; Curtiss, L.; Amine, K.; Sun, Y.-K.; Scrosati, B. Study on the catalytic activity of noble metal nanoparticles on reduced graphene oxide for oxygen evolution reactions in lithium-air batteries. *Nano Lett.* **2015**, *15*, 4261–4268. [[CrossRef](#)] [[PubMed](#)]
16. Yao, Y.; Wu, F. Turning Waste Chemicals into Wealth A New Approach to Synthesize Efficient Cathode Material for an Li-O₂ Battery. *ACS Appl. Mater. Interfaces* **2017**, *9*, 31907–31912. [[CrossRef](#)] [[PubMed](#)]
17. Zhang, S.; Wen, Z.; Rui, K.; Shen, C.; Lu, Y.; Yang, J. Graphene nanosheets loaded with Pt nanoparticles with enhanced electrochemical performance for sodium-oxygen batteries. *J. Mater. Chem. A* **2015**, *3*, 2568–2571. [[CrossRef](#)]
18. Yang, X.; Peng, C.; Hou, M.; Zhang, D.; Yang, B.; Xue, D.; Lei, Y.; Liang, F. Rational Design of Electrolyte Solvation Structures for Modulating 2e(-)/4e(-) Transfer in Sodium-Air Batteries. *Adv. Funct. Mater.* **2022**, *32*, 2201258. [[CrossRef](#)]
19. Li, M.; Wang, X.; Li, F.; Zheng, L.; Xu, J.; Yu, J. A Bifunctional Photo-Assisted Li-O₂ Battery Based on a Hierarchical Heterostructured Cathode. *Adv. Mater.* **2020**, *32*, e1907098. [[CrossRef](#)]
20. Feng, Y.; Xue, H.; Wang, T.; Gong, H.; Gao, B.; Xia, W.; Jiang, C.; Li, J.; Huang, X.; He, J. Enhanced Li₂O₂ Decomposition in Rechargeable Li-O₂ Battery by Incorporating WO₃ Nanowire Array Photocatalyst. *ACS Sustain. Chem. Eng.* **2019**, *7*, 5931–5939. [[CrossRef](#)]

21. Malathi, A.; Madhavan, J.; Ashokkumar, M.; Arunachalam, P. A review on BiVO₄ photocatalyst: Activity enhancement methods for solar photocatalytic applications. *Appl. Catal. A-Gen.* **2018**, *555*, 47–74.
22. Moniz, S.J.A.; Shevlin, S.A.; Martin, D.J.; Guo, Z.-X.; Tang, J. Visible-light driven heterojunction photocatalysts for water splitting—A critical review. *Energy Environ. Sci.* **2015**, *8*, 731–759. [[CrossRef](#)]
23. Ke, D.; Peng, T.; Ma, L.; Cai, P.; Dai, K. Effects of hydrothermal temperature on the microstructures of BiVO₄ and its photocatalytic O₂ evolution activity under visible light. *Inorg. Chem.* **2009**, *48*, 4685–4691. [[CrossRef](#)] [[PubMed](#)]
24. Tan, H.L.; Amal, R.; Ng, Y.H. Alternative strategies in improving the photocatalytic and photoelectrochemical activities of visible light-driven BiVO₄: A review. *J. Mater. Chem. A* **2017**, *5*, 16498–16521. [[CrossRef](#)]
25. Thalluri, S.M.; Hernández, S.; Bensaid, S.; Saracco, G.; Russo, N. Green-synthesized W- and Mo-doped BiVO₄ oriented along the {0 4 0} facet with enhanced activity for the sun-driven water oxidation. *Appl. Catal. B Environ.* **2016**, *180*, 630–636. [[CrossRef](#)]
26. Li, J.; Guo, L.; Lei, N.; Song, Q.; Liang, Z. Metallic Bi Nanocrystal-Modified Defective BiVO₄ Photoanodes with Exposed (040) Facets for Photoelectrochemical Water Splitting. *Chemelectrochem* **2017**, *4*, 2852–2861. [[CrossRef](#)]
27. Xu, X.; Xu, Y.; Xu, F.; Jiang, G.; Jian, J.; Yu, H.; Zhang, E.; Shchukin, D.; Kaskel, S.; Wang, H. Black BiVO₄: Size tailored synthesis, rich oxygen vacancies, and sodium storage performance. *J. Mater. Chem. A* **2020**, *8*, 1636–1645. [[CrossRef](#)]
28. Zhang, X.; Ai, Z.; Jia, F.; Zhang, L.; Fan, X.; Zou, Z. Selective synthesis and visible-light photocatalytic activities of BiVO₄ with different crystalline phases. *Mater. Chem. Phys.* **2007**, *103*, 162–167. [[CrossRef](#)]
29. Zhang, C.; Han, P.; Lu, X.; Mao, Q.; Qu, J.; Li, Y. Preparation and photocatalytic activity characterization of activated carbon fiber–BiVO₄ composites. *RSC Adv.* **2018**, *8*, 24665–24672. [[CrossRef](#)]
30. Rettie, A.J.; Lee, H.C.; Marshall, L.G.; Lin, J.F.; Capan, C.; Lindemuth, J.; McCloy, J.S.; Zhou, J.; Bard, A.J.; Mullins, C.B. Combined charge carrier transport and photoelectrochemical characterization of BiVO₄ single crystals: Intrinsic behavior of a complex metal oxide. *J. Am. Chem. Soc.* **2013**, *135*, 11389–11396. [[CrossRef](#)]
31. Wang, X.X.; Guan, D.H.; Li, F.; Li, M.L.; Zheng, L.J.; Xu, J.J. Magnetic and Optical Field Multi-Assisted Li–O₂ Batteries with Ultrahigh Energy Efficiency and Cycle Stability. *Adv. Mater.* **2022**, *34*, 2104792. [[CrossRef](#)] [[PubMed](#)]
32. Mamtani, K.; Jain, D.; Dogu, D.; Gustin, V.; Gunduz, S.; Co, A.C.; Ozkan, U.S. Insights into oxygen reduction reaction (ORR) and oxygen evolution reaction (OER) active sites for nitrogen-doped carbon nanostructures (CN_x) in acidic media. *Appl. Catal. B Environ.* **2018**, *220*, 88–97. [[CrossRef](#)]
33. Shang, M.S.; Liu, Y.; Xia, J.; Zhang, S.M.; Yang, J.H. Synthesis and characterization of MnCo₂O₄ microspheres based air electrode for rechargeable sodium-air batteries. *Ceram. Int.* **2017**, *43*, 3218–3223. [[CrossRef](#)]
34. Kim, Y.S.; Lee, G.H.; Sung, M.C.; Kim, D.W. Orthorhombically distorted perovskite SeZnO₃ nanosheets as an electrocatalyst for lithium-oxygen batteries. *Chem. Eng. J.* **2021**, *406*, 126896. [[CrossRef](#)]
35. Schroeder, D.; Bender, C.L.; Pinedo, R.; Bartuli, W.; Schwab, M.G.; Tomovic, Z.; Janek, J. How to Control the Discharge Product in Sodium-Oxygen Batteries: Proposing New Pathways for Sodium Peroxide Formation. *Energy Technol.* **2017**, *5*, 1242–1249. [[CrossRef](#)]
36. Kang, S.; Mo, Y.; Ong, S.P.; Ceder, G. Nanoscale Stabilization of Sodium Oxides: Implications for Na–O₂ Batteries. *Nano Lett.* **2014**, *14*, 1016–1020. [[CrossRef](#)]
37. Yang, S.; Siegel, D.J. Intrinsic Conductivity in Sodium-Air Battery Discharge Phases: Sodium Superoxide vs Sodium Peroxide. *Chem. Mater.* **2015**, *27*, 3852–3860. [[CrossRef](#)]
38. Bi, X.X.; Wang, R.Y.; Amine, K.; Lu, J. A Critical Review on Superoxide-Based Sodium-Oxygen Batteries. *Small Methods* **2019**, *3*, 1800247. [[CrossRef](#)]
39. Malashchonak, M.V.; Streltsov, E.A.; Kuliomin, D.A.; Kulak, A.I.; Mazanik, A.V. Monoclinic bismuth vanadate band gap determination by photoelectrochemical spectroscopy. *Mater. Chem. Phys.* **2017**, *201*, 189–193. [[CrossRef](#)]
40. Zhang, A.; Zhang, J. The effect of hydrothermal temperature on the synthesis of monoclinic bismuth vanadate powders. *Mater. Sci.* **2009**, *27*, 1015–1023.
41. Wellendorff, J.; Silbaugh, T.L.; Garcia-Pintos, D.; Norskov, J.K.; Bligaard, T.; Studt, F.; Campbell, C.T. A benchmark database for adsorption bond energies to transition metal surfaces and comparison to selected DFT functionals. *Surf. Sci.* **2015**, *640*, 36–44. [[CrossRef](#)]
42. Sun, Q.; Yadegari, H.; Banis, M.N.; Liu, J.; Xiao, B.; Wang, B.; Lawes, S.; Li, X.; Li, R.; Sun, X. Self-stacked nitrogen-doped carbon nanotubes as long-life air electrode for sodium-air batteries: Elucidating the evolution of discharge product morphology. *Nano Energy* **2015**, *12*, 698–708. [[CrossRef](#)]
43. Ryu, W.-H.; Gittleson, F.S.; Thomsen, J.M.; Li, J.; Schwab, M.J.; Brudvig, G.W.; Taylor, A.D. Heme biomolecule as redox mediator and oxygen shuttle for efficient charging of lithium-oxygen batteries. *Nat. Commun.* **2016**, *7*, 12925. [[CrossRef](#)]
44. Sun, Q.; Liu, J.; Xiao, B.; Wang, B.; Banis, M.; Yadegari, H.; Adair, K.R.; Li, R.; Sun, X. Visualizing the Oxidation Mechanism and Morphological Evolution of the Cubic-Shaped Superoxide Discharge Product in Na-Air Batteries. *Adv. Funct. Mater.* **2019**, *29*, 1808332. [[CrossRef](#)]
45. Jin, X.; Li, Y.; Zhang, S.; Zhang, J.; Shen, Z.; Zhong, C.; Cai, Z.; Hu, C.; Zhang, H. Ru single atoms induce surface-mediated discharge in Na–O₂ batteries. *Chin. Chem. Lett.* **2022**, *33*, 491–496. [[CrossRef](#)]
46. Yin, W.-W.; Shadike, Z.; Yang, Y.; Ding, F.; Sang, L.; Li, H.; Fu, Z.-W. A long-life Na-air battery based on a soluble NaI catalyst. *Chem. Commun.* **2015**, *51*, 2324–2327. [[CrossRef](#)]